Title
Experimental mapping of elastoplastic surfaces for sand using undrained perturbations

Journal
Soils and Foundations, 58(1)

ISSN
0385-1621

Authors
Eslami, Mohammad M
Pradel, Daniel
Brandenberg, Scott J

Publication Date
2018-02-01

DOI
10.1016/j.sandf.2017.12.004

Peer reviewed

Experimental Mapping of Elastoplastic Surfaces for Sand Using Undrained Perturbations

by Mohammad M. Eslami[1], Daniel Pradel[2], and Scott J. Brandenberg[3]

Abstract

Elastoplastic models are commonly used in modern geotechnical practice to numerically predict displacements, stresses, and pore pressures in large construction projects. These elastoplastic models use presumed functional forms for yield and plastic potential functions that are rarely obtained from experimental measurements. This research describes a simple experimental technique that can be used to obtain the slopes of the plastic potential and yield functions during shear based on the deformation theory of plasticity. The method imposes small perturbations in the direction of the stress increment by closing the drainage valve, thereby abruptly switching from drained to undrained loading conditions during plastic loading. Elastoplastic moduli are obtained immediately before and after the perturbation from the measured deviatoric stress, mean effective stress, deviatoric strains, and volumetric strains for the stress paths immediately before and immediately after closing the drain valve. During drained shear, samples were sheared while the mean effective stress was maintained constant. Combining tests performed at several confining stresses, the proposed method can map conventional isotropic yield and plastic potential surfaces and predict their evolution for a wide range of stresses. The proposed technique can also be used for kinematic yield surface and may be used to develop new and more accurate elastoplastic constitutive models.

[1] 2270 Boelter Hall, Department of Civil and Environmental Engineering, University of California, Los Angeles, CA 90095-1593.
[2] Hitchcock Hall, 2070 Neil Avenue, Department of Civil, Environmental, and Geologic Engineering, Ohio State University, Columbus, OH 43210
[3] 5731 Boelter Hall, Department of Civil and Environmental Engineering, University of California, Los Angeles, CA 90095-1593. Email: sjbrandenberg@ucla.edu. Corresponding author.

Keywords: soil plasticity, yield surface, plastic potential, plastic flow, constitutive modeling, non-associated flow, elastoplastic behavior.

Introduction

Using numerical simulations to predict permanent deformations caused by surcharges, excavations and other similar geotechnical loading mechanisms, requires constitutive models that successfully estimate the anticipated level of irrecoverable strains. The use of numerical modelling for the design of large geotechnical projects has become widespread in recent years, especially for large infrastructure projects such as dams, tunnels, and highway embankments, as well as for deep excavations next to existing buildings. The considerable importance of modelling in the analysis and design of geo-structures was acknowledged in 2010, when it was named one of the focus areas at the Geo-Institute's national conferences (ASCE, 2010).

Constitutive models commonly implemented in finite element computer programs, such as PLAXIS (2015) or finite difference programs such as FLAC (Itasca, 2011) are generally elastoplastic in nature and use single or dual isotropic yield surfaces. As illustrated in Fig. 1, commonly used models exhibit significant differences in the treatment of yield surfaces and plastic potential surfaces. The simplest models consist of a Mohr-Coulomb or Drucker-Prager type yield surface, with the plastic flow direction controlled by a constant dilation angle (Fig. 1a). These models neglect many fundamental features of soil behavior, including plastic volumetric flow under isotropic loading conditions (i.e., do not generate irrecoverable strains in isotropic consolidation), small-strain yielding, and critical state soil mechanics. Roscoe and Schofield (1963) introduced the original Cam-clay model (Fig. 1b), which utilizes a logarithmic function to define the yield surface in the q-p' stress invariant space, and an associated flow rule (i.e., the plastic potential surface and yield surface coincide). This model conforms to critical state soil mechanics, meaning that the failure condition is associated with zero volumetric strain rate as the plastic shear strains continue to accumulate, and it is capable of capturing consolidation behavior though its yield surface generates deviatoric strains under isotropic consolidation conditions. The modified Cam-clay model (Roscoe and Burland, 1968) uses an elliptic yield surface to eliminate deviatoric strains under isotropic loading conditions. Since the formulation of these yield surfaces is isotropic, their elastic region is quite large. To improve predictions for different stress increment directions, Vermeer (1978) developed a double-hardening model for sand consisting of a nonlinear surface for deviatoric yielding (non-associated) and a separate vertical surface (associated) for volumetric yielding (Fig. 1c). The formulation in Vermeer’s model is also isotropic and thus more appropriate for monotonic loading conditions. Lade and Kim developed a teardrop shaped model (Fig. 1d) that eliminated the sharp corner in Vermeer's double hardening model, and some of the associated return mapping difficulties at the cost of slightly less accurate predictions.

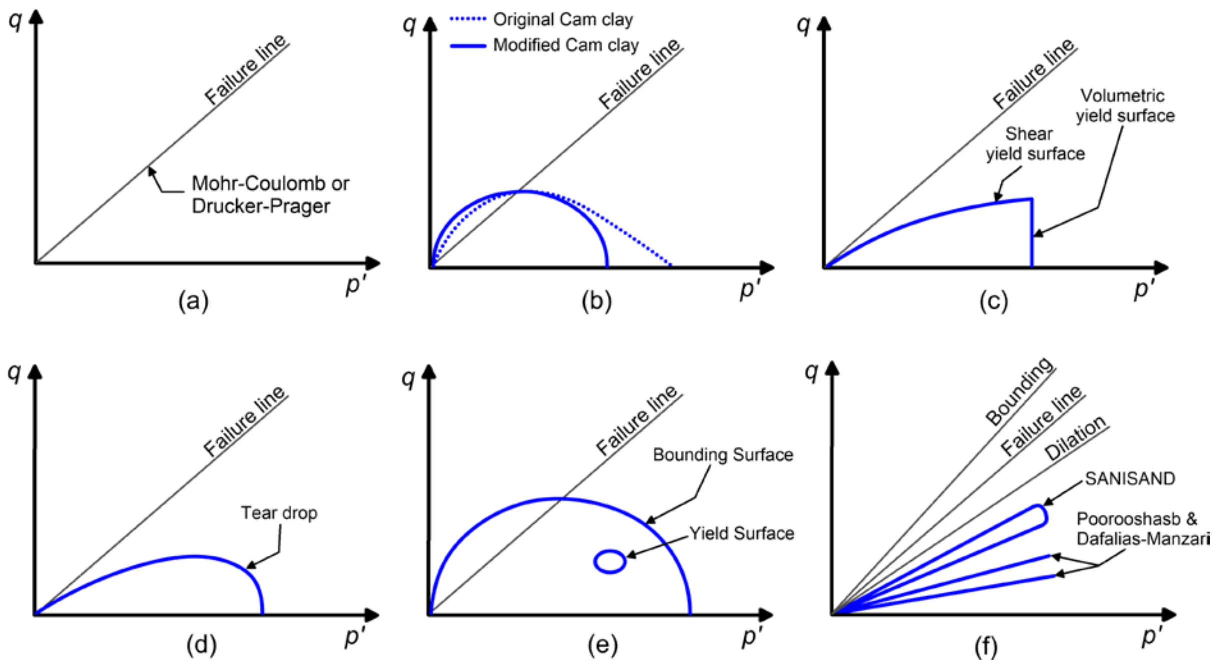

Fig. 1. Examples of yield surfaces, *f = 0*, used for geotechnical applications (a) Mohr-Coulomb and Drucker-Prager; (b) Original and modified Cam-clay (Roscoe and Schofield, 1963 and Roscoe and Burland, 1968); (c) Vermeer’s Double hardening model (Vermeer, 1978); (d) Tear drop shaped surface from Lade and Kim (1988), (e) Cam-clay bubble model (Al-Tabbaa and Muir Wood (1989), and (f) Drucker-Prager type kinematic hardening surfaces, Poorooshasb and Pietruszczak (1985), Dafalias and Manzari (2004), and SANISAND (Taiebat and Dafalias, 2008)

Yield surfaces that exhibit isotropic hardening, such as those in Figs. 1b, c, and d result in a large elastic region after significant yielding, rending the models inappropriate for reverse or cyclic loading conditions. To more accurately model cyclic behavior, Mróz et al. (1979) proposed a modeling technique based on kinematic hardening, that translates and rotates during loading, generally within the context of a larger bounding surface that exhibits isotropic and/or kinematic hardening (Fig. 1e). Examples include the Cam-clay bubble model developed by Al-Tabbaa and Muir Wood (1989) for clays (Fig. 1e) in which a small "bubble" yield surface moves inside of an isotropic bounding surface. Both the yield and bounding surfaces have the shape of the modified Cam-clay model. A similar approach for sands includes the Dafalias and Manzari (2004) model, that utilizes a small Drucker-Prager type yield surface, along with a Drucker-Prager type bounding surface, critical state line, and dilatancy surface (Fig. 1f). The model lacks a volumetric cap, and therefore exhibits only elastic volumetric strains upon loading at a constant stress ratio. Taiebat and Dafalias (2008) developed a SANISAND model that uses a rounded yield surface in conjunction with a Drucker-Prager type bounding surface that permits plastic volumetric strains upon loading at constant stress ratio (Fig. 1f). Since kinematic plasticity models often utilize an isotropic bounding surface formulation, and are often calibrated using monotonic tests, the yielding and plastic flow during monotonic loading is important to understand.

Interestingly, although the shape of their yield surfaces are notably different, all these models have been shown, by their authors, to produce reasonable predictions for monotonic conventional laboratory tests. It suggests that the input parameters can be tuned to compensate for differences between the experimental and theoretical yield surfaces and flow rules. The appropriateness of the slope of the yield surface is nevertheless very important for the accurate predictions of problems involving more complex stress paths. For instance, if a normally consolidated soil is subject to plastic shear loading followed by a significant increase in pore water pressure under sustained shear, the predicted behavior during the initial stress increment would be:

- Elastic according to Cam-clay (Fig. 1b) and conventional Cap (e.g., Baladi and Rohani, 1979) models;
- Plastic according to Double hardening, Dafalias and Poorooshasb models (Figs. 1c and 1d), which would result in irrecoverable strains.
- Elastic or plastic depending on the stress level according to models having tear-drop shaped surfaces (Fig. 1e).

Experimental Studies to Measure Yield and Plastic Potential Surfaces

Although numerous expressions have been proposed for the yield surface ($f = 0$) and plastic potential ($g = 0$) by geotechnical researchers, there are relatively few experimental studies that have attempted to determine their actual shape. Previous experimental studies can be classified according to the following categories:

1. Tests containing cycles of loading, unloading and reloading (e.g., Poorooshasb et al., 1966 and 1967, Poorooshasb, 1971, Tatsuoka and Ishihara, 1974, Tatsuoka and Molenkamp, 1983, Pradel et al., 1990, Yasufuku et al., 1991, and Nawir et al., 2003), as exemplified in Fig. 2;
2. Acoustic emission tests (e.g., Tanimoto et al., 1986);
3. Tests in which the strain path is suddenly changed and plastic strains, slopes as well as moduli are calculated (e.g., Pradel and Lade, 1990, Kuwano and Jardine, 2007);

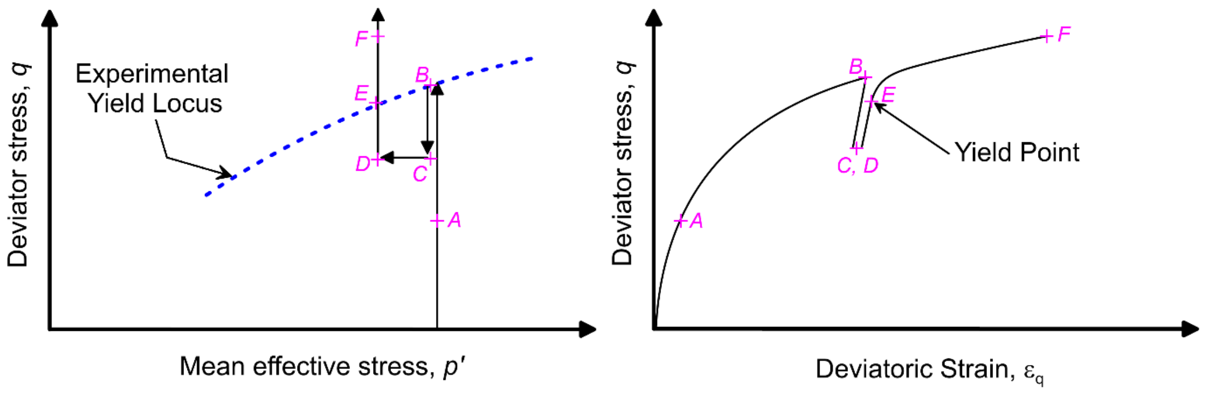

Fig. 2. Test with cycles of loading and unloading used for the determination of the yield surface

Generally, studies belonging to the first group have been used to investigate what Tatsuoka (2006) describes as "large-scale shear yielding", and have produced open-type yield surfaces with shapes that are similar to the ones in Figs. 1c and 1e. Size and mode of shearing can affect the yield surfaces as cautioned in Tatsuoka and Molenkamp (1983). More recent studies by Nawir et al. (2003) have focused on viscous effects by imposing distinct strain rates during cycles of loading and reloading. The method is powerful, however, the tests necessary tend to be numerous, complex, and require careful interpretation. Interpretation can be especially difficult when:

- The mean effective stress, p', increases significantly, which results in both shear and volumetric yielding mechanisms according to double hardening models (Fig. 1c);
- The unloading cycles produce large loops and irrecoverable strains;
- Yielding occurs near the failure line and mobilizes large strains.

The use of acoustic emissions to determine the shape of the yield surface requires not only specialized equipment (e.g., Tanimoto and Tanaka, 1986), but also requires sufficient noise generated by slippage and/or crushing of soil particles to accurately differentiate ambient noise from the acoustic emissions generated by yielding. Hence, the contributions from this methodology have been relatively limited.

The third methodology was used by Kuwano and Jardine (2007) to study kinematic yielding and Pradel and Lade (1990) to study the conditions leading to static liquefaction of saturated and partly saturated sands at a specific state of stress. Both studies involved a large number of tests. For example, Pradel and Lade (1990) used a total of four triaxial tests from which moduli were measured to obtain the slopes of the yield and plastic potential surfaces at a single point in the q - p' plane. Hence, the applicability of these methods to a wide range of stresses is generally not practical.

The main purpose of the present study is to extend the work by Pradel and Lade (1990) to experimentally obtain the slopes of the yield and plastic potential surfaces. This method is based on the incremental formulation of the deformation (or flow) theory of plasticity, and incorporates short undrained perturbations during a drained triaxial test with a vertical stress path. The tests can be performed on a traditional triaxial compression testing device without the need for specialized equipment, which makes the method attractive for routine use.

Incremental Formulation and Theoretical Background

The deformation theory of plasticity (e.g., Jones, 2009 and Wood, 1990) postulates that strains can be decomposed into elastic (fully recoverable) and plastic (irrecoverable) components. For a time-independent material this postulate is expressed incrementally as in Eq. 1.

$$d\varepsilon_{ij} = d\varepsilon_{ij}^{e} + d\varepsilon_{ij}^{p} \tag{1}$$

The theory of plasticity also postulates that a boundary exists in the stress space between elastic and plastic behavior. This boundary, namely the yield surface, is defined by a mathematical function, *f*, that describes a convex surface in the six-dimensional stress space as $f(\sigma_{ij}) = 0$. During loading (yielding), the direction of the plastic strain increments is perpendicular to a plastic potential surface, defined by a mathematical function, *g*, as $g(\sigma_{ij}) = 0$. Plastic loading resulting from an effective stress increment, $d\sigma_{ij}$, results in the plastic strain increment given in Eq. 2 (Pradel and Lade, 1990).

$$d\varepsilon_{ij}^{p} = \frac{1}{h}\frac{\partial g}{\partial \sigma_{ij}^{'}}\frac{\partial f}{\partial \sigma_{kl}^{'}}d\sigma_{kl}^{'} \tag{2}$$

Where, h, is the plastic hardening modulus (which is a function of hardening variables such as void ratio, previous stress history, stress and strain invariants, etc.).

In most elastoplastic models, the surfaces f and g are expressed in terms of invariants, and for conventional triaxial compression tests these surfaces can be defined uniquely in terms of the stress invariants provided in Eq. 3. Where p' is mean effective stress and q is the deviatoric stress.

$$p' = \frac{1}{3}\left(\sigma_1^{'} + \sigma_2^{'} + \sigma_3^{'}\right) \tag{3a}$$

$$q = \sqrt{\frac{1}{2}\left[\left(\sigma_1 - \sigma_2\right)^2 + \left(\sigma_1 - \sigma_3\right)^2 + \left(\sigma_2 - \sigma_3\right)^2\right]} \tag{3b}$$

Similarly, the volumetric and deviatoric strain invariants are defined as:

$$\varepsilon_v = \varepsilon_1 + \varepsilon_2 + \varepsilon_3 \tag{4a}$$

$$\varepsilon_q = \frac{2}{3}\sqrt{\frac{1}{2}\left[\left(\varepsilon_1 - \varepsilon_2\right)^2 + \left(\varepsilon_1 - \varepsilon_3\right)^2 + \left(\varepsilon_2 - \varepsilon_3\right)^2\right]} \tag{4b}$$

Elastic deviatoric and volumetric and strains can be computed using G and K, the elastic shear and bulk moduli using Eqs. 5 (a) and (b), respectively.

$$d\varepsilon_q^e = \frac{dq}{3G} \tag{5a}$$

$$d\varepsilon_v^e = \frac{dp'}{K} \tag{5b}$$

The introduction of local linear approximations for the yield surface (e.g., $f = q - \mu . p' - I_f = 0$) and plastic potential (e.g., $g = q - \eta_{pp} . p' - I_g = 0$), adopted from Fig. 3, into equation (2) provides the expressions provided in Eqs. (6a) and (6b), for the deviatoric and volumetric strains during plastic loading, respectively. Note that the I_f and I_g are intercepts of the slope of the yield surface and the plastic potential with the y-axis in Fig. 3.

$$d\varepsilon_q^p = \frac{1}{h}\frac{\partial g}{\partial q}\left(\frac{\partial f}{\partial q}dq + \frac{\partial f}{\partial p'}dp'\right) = \frac{1}{h}\left(dq - \mu \cdot dp'\right) \tag{6a}$$

$$d\varepsilon_v^p = \frac{1}{h}\frac{\partial g}{\partial p'}\left(\frac{\partial f}{\partial q}dq + \frac{\partial f}{\partial p'}dp'\right) = \frac{-\eta_{pp}}{h}\left(dq - \mu \cdot dp'\right) \tag{6b}$$

Where μ and η_{pp} are tangent slopes of the yield and plastic potential surfaces in the q - p' plane at the current stress point, shown in Fig. 3. As presented by Pradel and Lade (1990), the total strains are obtained by summing the elastic and plastic strain increments, provided in Eq. 7.

$$\begin{pmatrix} d\varepsilon_q \\ d\varepsilon_v \end{pmatrix} = \begin{pmatrix} \left(\frac{1}{3G} + \frac{1}{h}\right) & \frac{-\mu}{h} \\ \frac{-\eta_{pp}}{h} & \left(\frac{1}{K} + \frac{\mu \cdot \eta_{pp}}{h}\right) \end{pmatrix} \cdot \begin{pmatrix} dq \\ dp' \end{pmatrix} \tag{7}$$

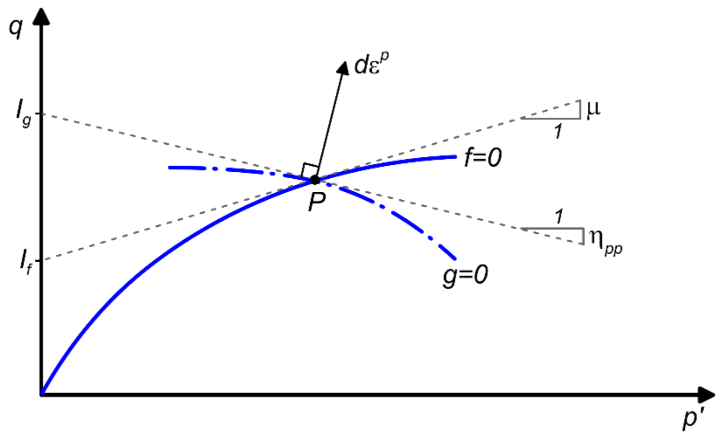

Fig. 3. Schematic representation of the yield surface, plastic potential and the gradients to these surfaces and the plastic strain increment at point *P* in the triaxial space

Experimental Application

During loading equation (7) provides two equations that are derived from the five elastoplastic material properties: G, K, h, μ, and η_{pp}. Though Eq. 7 is strictly applicable at a single point, it is approximately valid for small stress increments within the region where the linearized form is approximately equivalent to the surfaces. To measure these properties, first the elastic moduli, G and K, are measured using small volumetric and deviatoric load paths, or another suitable means such as bender element tests. Because G and K depend on p' for soil, maintaining a constant value of p' is advantageous during shearing. To measure h, μ, and η_{pp}, a triaxial compression test (as illustrated in Fig. 4) is performed using the following steps:

1. A vertical stress path is first applied under drained loading conditions (points A to B in Fig. 4), and values of $d\varepsilon_q$, $d\varepsilon_v$, and dq are measured;
2. The drain valve is closed to provide a small undrained perturbation (e.g., between points B to C in Fig. 4), and values of $d\varepsilon_q$, dq, and dp' are measured.
3. The drain valve is slowly opened (at point C).

The process described above is repeated at multiple points along the stress path.

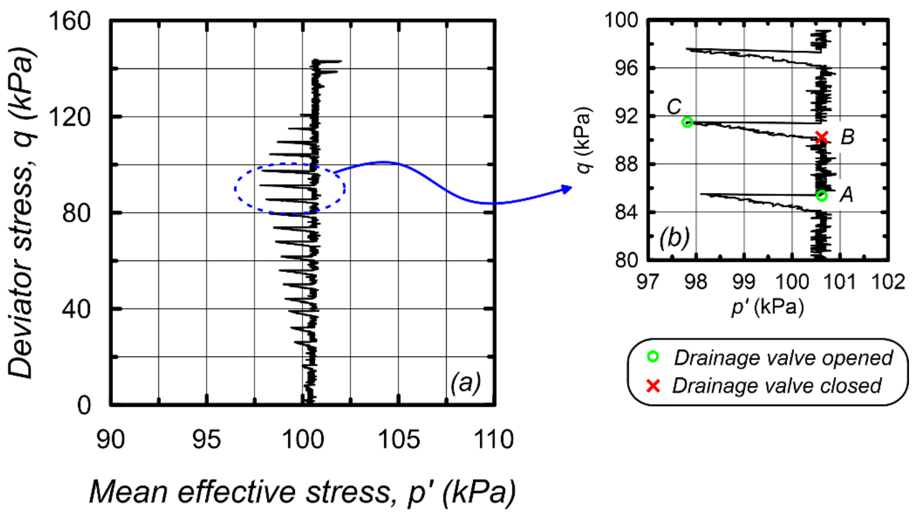

Fig. 4. Stress path of drained p′ constant triaxial test with a short undrained portion (note that the scale of the horizontal axis has been stretched for illustrative purposes)

During the drained shearing phase, values of h and η_{pp} are computed using Eqs. 8 and 9, respectively, which are obtained by solving Eq. 7 with $dp' = 0$.

$$h = \frac{1}{\dfrac{d\varepsilon_q}{dq} - \dfrac{1}{3G}} \tag{8}$$

$$\eta_{pp} = -\frac{d\varepsilon_v}{dq} h \tag{9}$$

The value of μ is solved from the undrained loading phase using Eq. 10, obtained after making appropriate substitutions into the portion of Eq. 7 corresponding to $d\varepsilon_q$ (i.e., the top line in the equation), and using the value of h from Eq. 8.

$$\mu = \left[\left(1 + \frac{h}{3G} \right) \frac{dq}{dp'} - \frac{d\varepsilon_q}{dp'} \right] \tag{10}$$

Note that $d\varepsilon_v = 0$ for undrained loading (i.e., the bottom line of Eq. 7) provides an expression for a residual that should equal zero, and therefore provides a means of assessing the quality of the measurements. The resulting residual equation is given by Eq. 11.

$$0 \approx \mathrm{R} = \frac{-\eta_{pp}}{h} dq + \left(\frac{1}{K} + \frac{\mu \cdot \eta_{pp}}{h} \right) dp \tag{11}$$

Experimental Results

A GCTS STX-50 pneumatic triaxial device was utilized to perform the experiments presented herein. The device is equipped with an internal load cell so that friction between the piston and the bushing is not included in the vertical force measurement. Vertical displacements were measured using an LVDT mounted on the piston outside of the cell. Volume change was measured by a differential pressure transducer measuring the difference in pressure between the top and bottom of the burette. The stock burettes that come with the device have a diameter of 17.4 mm, which is rather large. To enhance the accuracy of the volume change measurements, a smaller burette with a diameter of 6.3 mm was installed on the device. Pore pressure was measured using a pressure transducer installed between the bottom of the specimen and the valve on the line coming out of the cell. This position avoids errors in volume change arising from volumetric compliance of the plastic tubes connecting the specimen to the burettes.

The cylindrical specimens had a height of 150mm and a diameter of 71mm. The rubber latex membranes used were 0.5mm thick. The top and bottom platens of the triaxial apparatus were not lubricated, which may contribute to experimental errors due to shear stresses on the top and bottom surfaces. Membrane penetration was not measured, but is expected to be small because the sand is fine relative to the membrane thickness. More detailed documentation on laboratory procedures are provided in Eslami (2017).

The triaxial test configuration utilized herein is fairly standard, and can be replicated in many laboratories. This makes the procedure presented herein approachable for routine application. The influence of measurement errors is quantified by calculating confidence limits on the computed plasticity parameters. The confidence limits include the influence of measurement noise on the computed quantities. More advanced measurement techniques, such as internal displacement or strain measurements, lubricated top and bottom caps, or image analysis of the surface displacement field could improve the data quality, thereby reducing the range of the confidence limits. Although these techniques are common in Japanese laboratories they are less common in the US and other countries, and were not applied in the current study.

The experimental results derived from this study are curated, published (Eslami et al. 2017), and available for re-use in DesignSafe-CI, a platform for natural hazards research (Rathje et al., 2017). The interactive data curation and publication pipelines permits assigning categories to data to represent the primary processes of engineering experiments (Esteva et al., 2016). The dataset contains the experimental data, as well as more detailed documentation on laboratory procedures. A Jupyter notebook is also included to facilitate visualization of the data.

Tested Material and Sample Preparation

The material tested was a clean "Orange County Silica sand-mesh 60", with a mean grain size D_{50}, of 0.3 mm, a coefficient of uniformity $C_u = 2$ and a coefficient of curvature $C_c = 1.24$. This sand classifies as SP according to the Unified Soil Classification System (ASTM D2487). The minimum and maximum void ratios for the sand were $e_{min} = 0.792$ and $e_{max} = 0.958$. The slope of the yield surface depends on the measurement of pore pressure change during small undrained perturbations. To enhance the pore pressure response, the specimens were prepared as loose as possible. A plastic tube with a fine mesh at the bottom was first inserted into the specimen mold with the mesh resting on the bottom porous stone. The outside diameter of the tube was slightly smaller than the inside diameter of the triaxial mold. Dry sand was then placed into the plastic tube, and the tube was raised very slowly so that the sand particles were pluviated at essentially zero drop-height. The average void ratio of the dry samples prior to consolidation was 0.955, which corresponds to a relative density of about 2% prior to testing. The samples were subsequently isotropically consolidated, which caused the relative density to increase slightly but still remain under 10%. Samples were flushed with CO_2 prior to saturation with de-aired water, and back pressure saturation was used to achieve B-values larger than 95%. The average saturated unit weight of the samples was 18.1 kN/m^3, and their dry unit weight was on average 13.3 kN/m^3.

Elastic Moduli

To measure the elastic bulk modulus, K, a specimen was isotropically consolidated to 100 kPa, and the cell pressure was then cyclically reduced to 80 kPa and increased to 100 kPa while the volume change was recorded using a differential pressure transducer. The bulk modulus was computed using Eq. 5b. This process was repeated as the specimen was isotropically consolidated to 200, 300, 400, 300, 200, and 100 kPa. The resulting bulk modulus values are plotted in Fig. 5. A least-squares regression was performed to relate bulk modulus to mean effective stress, as indicated in Eq. 12a, where p_a = 101.325 kPa.

To measure shear modulus, two methods were considered. First, the Young's modulus, *E*, was measured by imposing 0.01% amplitude cyclic axial strain cycles, computing the slope by least squares regression, and subsequently computing shear modulus as $G = 3KE/(9K\text{-}E)$, in accordance with homogeneous isotropic linear elasticity theory, where the measured values of *K* and *E* corresponding to each consolidation pressure were used. This method is not particularly accurate because (1) the cyclic strain amplitude is large enough that the measured response is a combination of elastic and plastic behavior, and separating the two responses requires additional assumptions, and (2) sensor noise contributed significantly to the measurements because 0.01% is close to the resolution limit for the load cell and LVDT. Therefore, the shear modulus was measured using bender elements embedded in the sand using a custom-made consolidation ring. Vertical pressures were applied to the sand, the source bender element was excited by a step wave function, and the travel time was selected based on the received signal following procedures outlined by Brandenberg et al. (2008). The bender element excitations are very small strain, and therefore act in the elastic region of the soil. The measurements were then regressed to obtain Eq. 12(b). The adopted values of the shear modulus are shown in Eq. 12b and Figure 5.

$$K = 50{,}600kPa\left(\frac{p'}{p_a}\right)^{0.78} \tag{12a}$$

$$G = 37,800kPa\left(\frac{p'}{p_a}\right)^{0.56} \tag{12b}$$

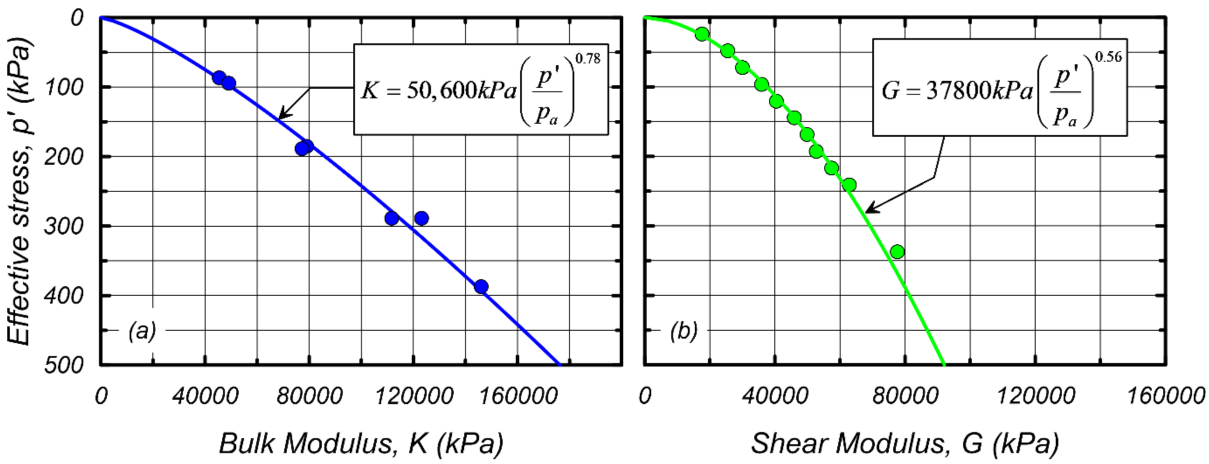

Fig. 5. Measurements of elastic moduli experiment: (a) bulk modulus measurements and adopted correlation, (b) Shear modulus measurements and correlation

Shear Testing

Testing was conducted for mean effective consolidation stress values of p' = 100, 150, 200, 250, 300, 350 and 400 kPa, and the resulting stress paths are plotted in Fig. 6. Constant mean effective stress conditions were obtained using stress-controlled loading and by decreasing the cell pressure as follows: $\Delta\sigma_3 = -\,q/3$. A computer control system was utilized to achieve the desired stress path. During drained loading, the drain tap connected to the specimen was periodically closed to impose a small undrained loading perturbation on the specimen. These perturbations manifest as sudden changes in p' apparent in Fig. 6. The drain tap was left closed until adequate pore pressure response had been recorded, and subsequently re-opened very slowly to proceed with drained loading. Approximately 20 to 25 perturbations were imposed on each specimen. The perturbations resulted in a small reduction in p' at low stress ratios where the specimens were contractive. However, the specimens became slightly dilative at stress ratios (q / p') higher than about M^d = 1.3 (Fig. 6a).

Note that M^d is the stress ratio at the transition from contractive to dilative behavior. The tests reached deviatoric strains of 10%, at which point the deviatoric stress and void ratio were still changing as deviatoric strain increased, indicating that the specimens did not reach a critical state condition. The stress ratio at a strain of 10% was $M = q / p' = 1.4$, which is associated with a friction angle of $\phi = 34°$, where $M = 6\sin\phi/(3-\sin\phi)$.

The values of dq/dp', $d\varepsilon_q/dp'$, $d\varepsilon_q/dq$, and $d\varepsilon_v/dq$ required to solve for h, η_{pp}, and μ using Eqs. 8, 9, and 10, respectively, were obtained as illustrated in Fig. 7 for one of the perturbations conducted at a consolidation stress of 400 kPa. The quantities were first plotted versus time, and the rates of change of each quantity were computed using linear least squares regression for the load increment both the drained and undrained portions of loading. The rate dp'/dt was set to zero during drained loading and $d\varepsilon_v/dt$ was set to zero for undrained loading. The desired ratios were then computed as the ratio of the rates [e.g., $dq/dp' = (dq/dt)/(dp'/dt)$]. The number of data points extracted for linear least squares regression depended on the amount of nonlinearity in the soil response. Near the beginning of each test (i.e., at low stress ratio) more data points were utilized because the strains evolved more slowly than later in the test. Recall that stress control was required to maintain a vertical stress path, therefore the strain rate tended to increase with time as the soil became softer.

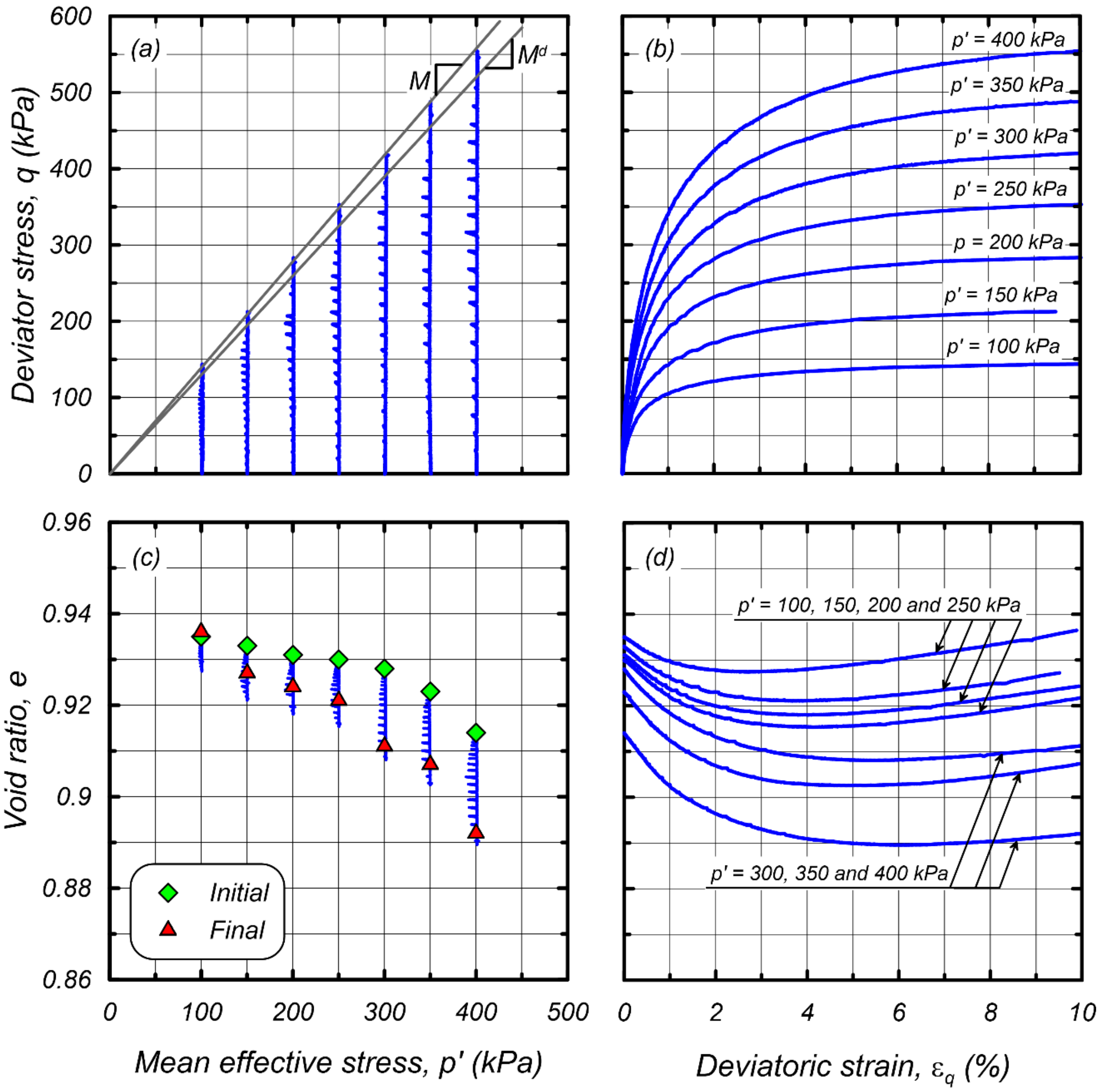

Fig. 6. General soil behavior of 7 triaxial compression tests: (a) effective stress paths, (b) stress-strain curves, (c) void ratio vs. mean effective stress, (d) void ratio vs. deviatoric strain curves

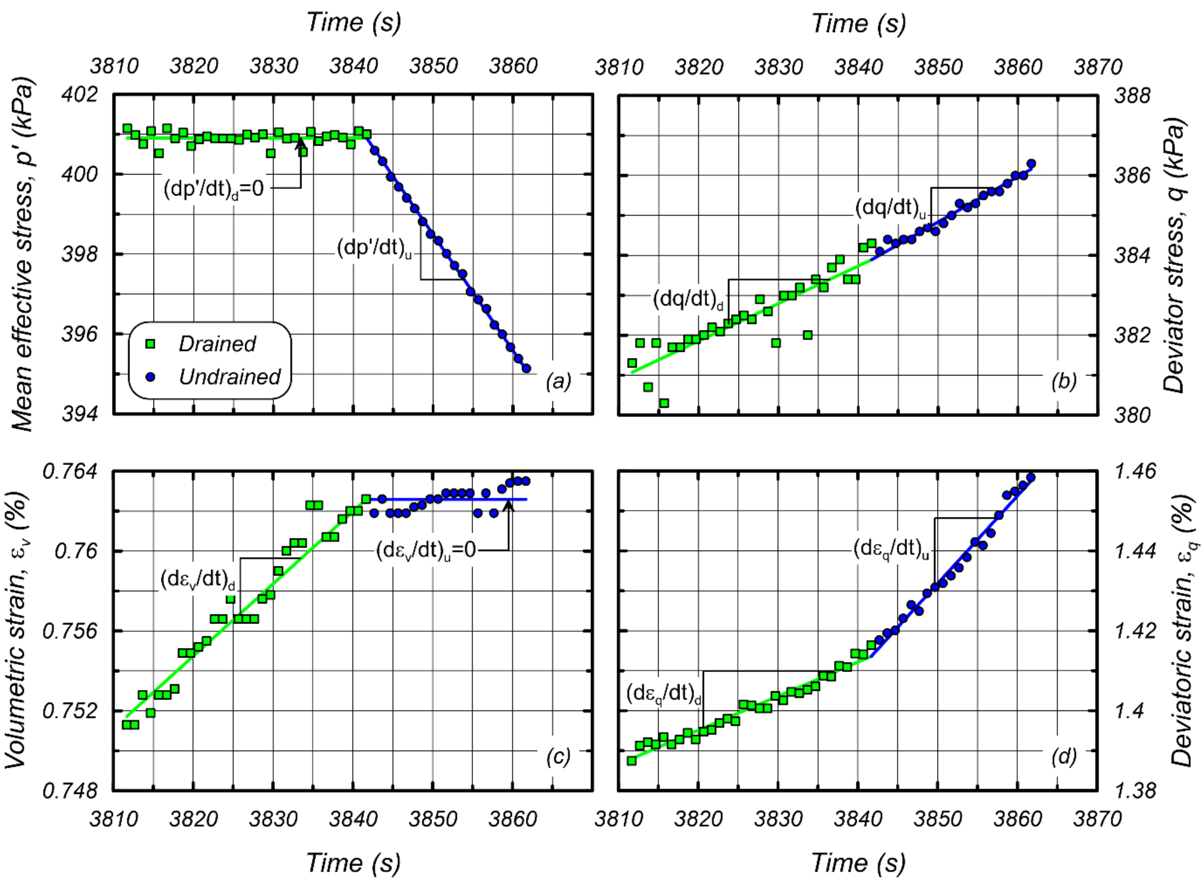

Fig. 7. Example data during one perturbation for the specimen consolidated at 400 kPa. Data quantities are (a) mean effective stress, (b) deviator stress, (c) volumetric strain, and (d) deviatoric strain.

Plastic Modulus

A value of plastic modulus was computed from the drained loading stages based on Eq. 8 at each point where an undrained perturbation was imposed on the specimen. The resulting plastic modulus values were subsequently normalized by $3G$, and plotted in Fig. 8. Plastic modulus is known to depend on shear modulus (e.g., Dafalias and Manzari, 2004), hence normalizing the plastic modulus results in a relationship that is independent of p'. The 95% confidence limits indicate that the measurements were of poorer quality at low stress ratio than at high stress ratio. This is due to the fact that deviatoric strain increments are quite small at low stress ratio, therefore signal noise influences the measurement of h. A weighted least squares regression was performed to arrive at Eq. 13, where weights were assigned to be inversely proportional to the 95% confidence limit range.

$$\frac{h}{3G} = 0.12 \frac{1.4 - \eta}{\eta} \tag{13}$$

The functional form of the expression above, assumes that plastic modulus is inversely proportional to the distance from the current point in q-p' space to the failure line, M. This loosely follows Dafalias and Manzari (2004), with the exception that they compute plastic modulus as a function of distance to the bounding surface, which in turn depends on the state parameter. The constants 1.4 and 0.12 are analogous to the parameters M^b (the bounding or "image" stress ratio on the bounding surface) and b_0 (a parameter that defines the plastic modulus at the initiation of the loading process) in Dafalias and Manzari (2004), respectively.

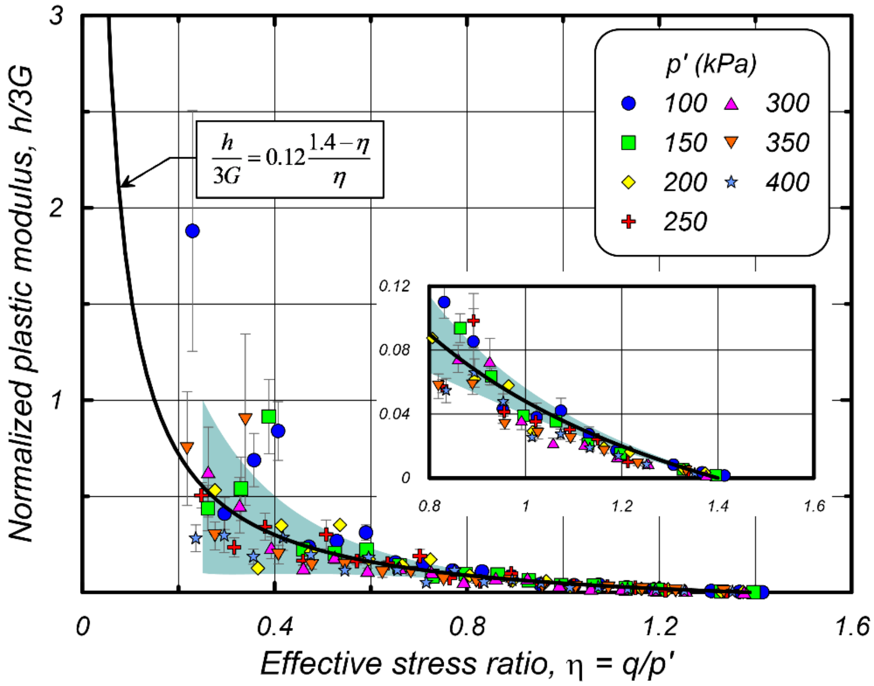

Fig. 8. Normalized plastic modulus ($h/3G$) versus stress ratio ($\eta = q / p'$). Vertical bars are 95% confidence limits and shaded region corresponds to ± one standard deviation of the residuals.

Plastic Potential Slope

The slope of the plastic potential surface, η_{pp}, was computed for each undrained perturbation, and the results are plotted versus the stress ratio $\eta = q/p'$ in Fig. 9. A negative slope of the plastic potential surface indicates contractive behavior, while a positive slope indicates dilation.

The sand is contractive essentially over the full range of loading, and is the most highly contractive at a stress ratio near 0.4. Superposed on the data are the slopes of the plastic potential surfaces associated with the original and modified Cam-clay models (Schofield and Wroth, 1968, and Roscoe and Burland, 1968). Although the Cam-clay model was formulated for clay and not for sand, the sand tested herein appears to exhibit characteristics that are qualitatively similar to the Cam-clay model. This does not mean that the Cam-clay model is appropriate for sands because the compressibility behavior may in fact be significantly different. The original Cam-clay model has a slope that varies linearly with η, and fits the observed data reasonably well at stress ratios higher than about 0.8, but lies beneath the data at lower stress ratios. The modified Cam-clay model lies significantly below the data. A weighted least squares regression was performed on the data, resulting in the expression given in equation (14).

$$\eta_{pp} = -0.177 + 0.599 \cdot \ln(\eta) \tag{14}$$

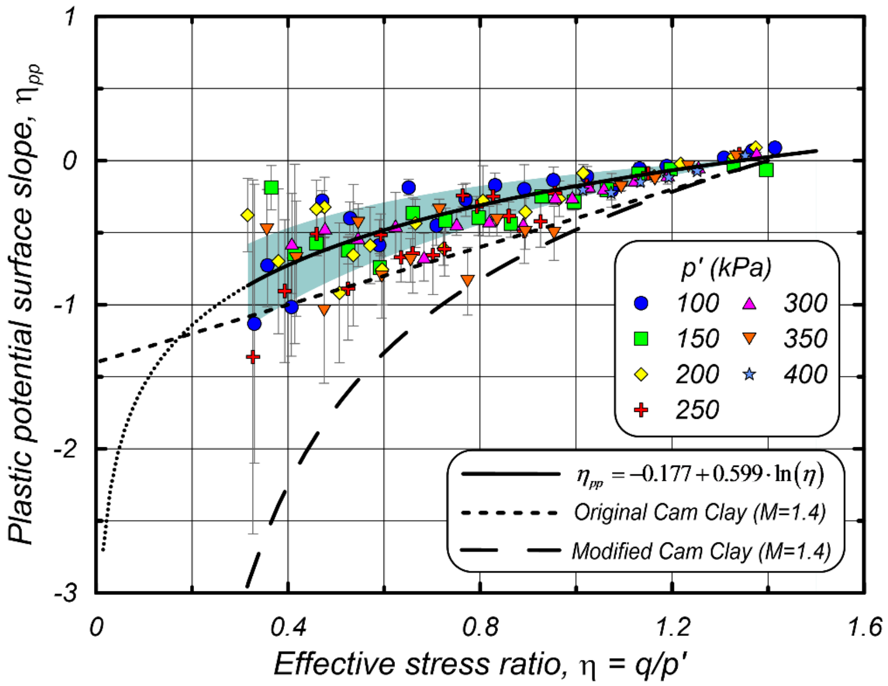

Fig. 9. Slope of plastic potential surface, η_{pp}, versus effective stress ratio ($\eta = q / p'$). Vertical bars are 95% confidence limits and shaded region corresponds to ± one standard deviation of the residuals.

Flow behavior is known to depend not only on stress ratio, but also on the void ratio relative to the critical state void ratio, which is commonly quantified by the state parameter $\psi = e - e_c$. For example, the tested specimens were more highly contractive at high p' where ψ was largest (Fig. 6c). To account for the influence of soil state on plastic flow, the plastic potential surface must be a function not only of η, but also ψ. The data were therefore regressed according to the functional form in Eq. 15 (following Dafalias and Manzari 2004), with the results: $A_d = 0.61$ and $n_d = 11.2$. Since the specimens did not reach critical state, the critical state void ratio is unknown. For simplicity, the state parameter was therefore computed as the difference between the current void ratio and final void ratio for the test. Furthermore, $M = 1.4$ was used.

$$\eta_{pp} = -A_d \left[M \cdot \exp\left(n_d \cdot \psi \right) - \eta \right] \tag{15}$$

Yield Surface Slope

The slope of the yield surface is plotted versus stress ratio in Fig. 10. The yield surface is negative at low stress ratio, and increases with stress ratio becoming positive at about $\eta = 1.1$. The 95% confidence limits are larger for the yield surface slope than for the plastic potential slope because the yield surface slope calculation utilizes volumetric strain, which is a comparatively noisy measurement, and carries over measurement errors from h and η_{pp}. A weighted least squares regression results in Eq. 16.

$$\mu = 0.012 + 0.331 \cdot \ln(\eta) \tag{16}$$

Eq. 16 differs from Eq. 14, which indicates that the sand exhibits a non-associated flow rule. For comparison, the Modified Cam-clay (M=1.4), Original Cam-clay (M = 1.4), and Drucker Prager yield surfaces are provided in Fig. 10. Note that the slope of the Drucker-Prager yield surface must be equal to the stress ratio for cohesionless material during yielding. None of these yield surfaces provide a particularly suitable match to the experimental data.

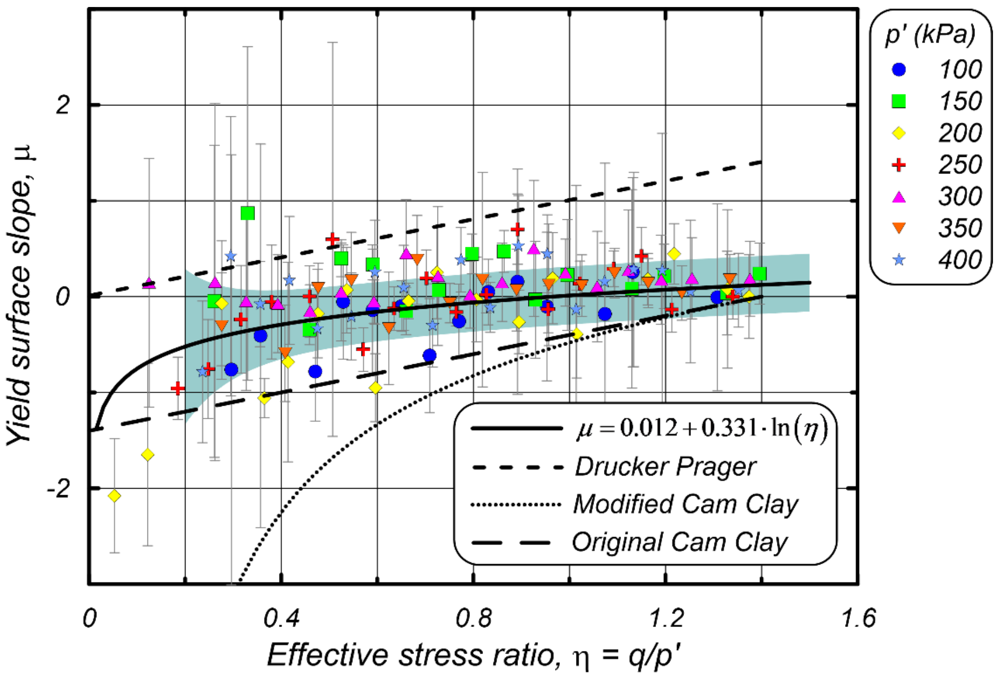

Fig. 10. Slope of yield surface, μ, versus effective stress ratio ($\eta = q / p'$). Vertical bars are 95% confidence limits and shaded region corresponds to ± one standard deviation of the residuals.

Residuals

Residuals computed using Eq. 11 are plotted in Fig. 11, and have units of volumetric strain. If the data quantities were measured perfectly, these residual values would be zero. The mean value of the residuals is 8.7e-6, and the standard deviation is 3.3e-5. These numbers are rather small compared with the measurement accuracy of the volume change sensor. For example, the noise amplitude of the volume change sensor is about 2.1e-5, which is close to the standard deviation of the residuals. This is an indication that we have extracted as much as possible from the data considering the limitations of the measurements. Any systematic errors (e.g., if the soil response were nonlinear within the range of measurements extracted for data processing) would cause these residuals to be higher than the noise levels of the volume change sensor.

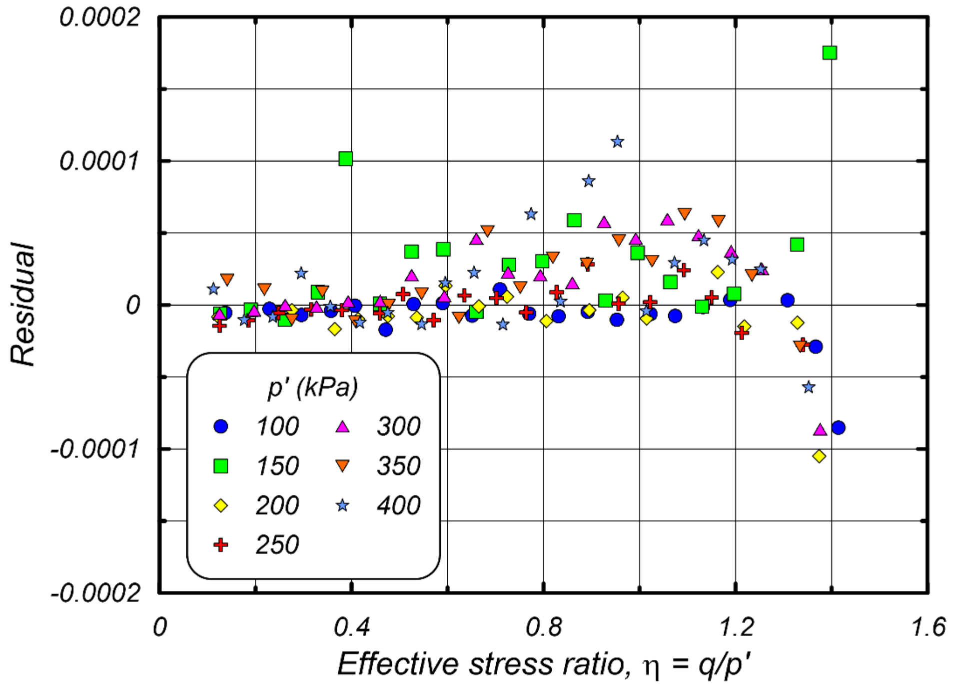

Figure 11. Residuals, R, computed using Eq. 13 versus effective stress ratio (η = q/p')

Interpretation of Data

The experimental data provide insights into the slopes of the yield and plastic potential functions. Equations 14, 15, and 16 provide these slopes at a particular point in stress space, and assumptions are required to sketch the yield or plastic potential surface. The simplest approach for interpreting the data is to assign a point in stress space, compute the desired slope at this point, and integrate the slope over a range of stress ratios to sketch the rest of the surface. This inherently assumes that the surfaces enclose an increasingly large elastic region as loading progresses (i.e., isotropic hardening). This assumption is similar to many traditional elastoplastic models such as Cam-clay. An example of this approach is illustrated in Fig. 12 for a vertical stress path at p' = 200 kPa, where yield surfaces are sketched at three different points along the stress path. These lines were obtained by numerically integrating Eq. 16. The shape of the surfaces is qualitatively similar to the original Cam-clay model in that the surfaces are curved and skewed to the left. The yield surfaces in Fig. 12 are drawn only in regions that lie reasonably within the bounds of experimental validation. Vectors indicating the directions of plastic flow that were measured, and computed using Eqs. 14 and 15 are also shown in Fig. 12 at the points where the stress path intersects the yield surface. The plastic flow vectors are not tangent to the yield surfaces at these points due to the non-associated flow rule.

Traditional isotropic hardening models provide reasonable predictions for monotonic loading, but results in a large elastic region that is inappropriate for cyclic loading. Models that utilize small yield surfaces that exhibit kinematic hardening are better suited to capture inelasticity in the reverse direction. For example, SANISAND (Taiebat and Dafalias, 2008) utilizes a narrow closed cone-type yield surface given by Eq. 17. This yield surface equation can be calibrated to match the experimental data by setting the parameters n and m, and solving for α and p_0 that provides the desired yield surface slope at a specific point in stress space. Note that α is the rotational hardening backstress ratio, p_0 is the isotropic hardening variable, m is the tangent of half the opening angle of the yield surface, and the exponent n introduces the effect of a cap-like shape at the tip of the yield surface. SANISAND yield surfaces are shown in Fig. 12 for m = 0.5 and n = 20. These surfaces intersect the isotropic hardening yield surfaces at the same points and with the same slopes, and provide an alternative interpretation that is equally consistent with the experimental data.

$$f = \left(q - p\alpha\right)^2 - m^2 p^2 \left[1 - \left(\frac{p}{p_0}\right)^n\right] = 0 \tag{17}$$

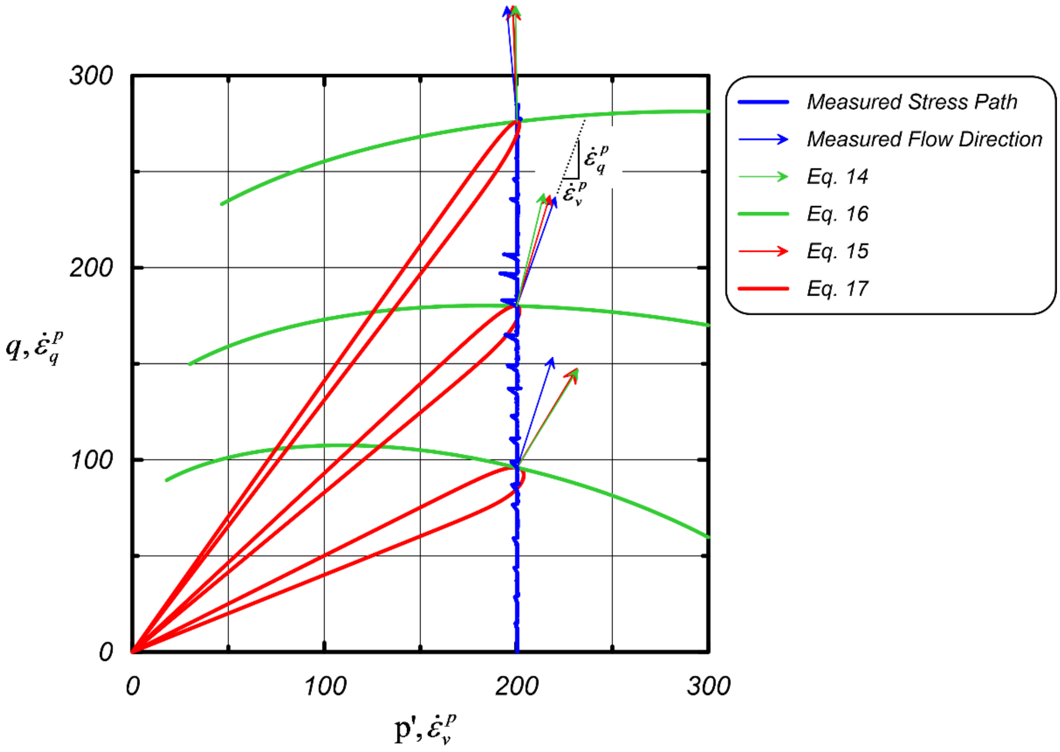

Fig. 12. Yield and plastic potential surfaces consistent with the experimental data for a vertical stress path at $\boldsymbol{p'}$ **= 200 kPa**

Elastoplastic functions are known to be dependent on loading rate effects. This has been shown by experimental studies such as Nawir et al. (2003) by mapping the shear yield surface by changing the strain rate during shear, suggesting that viscous properties be considered for realistic constitutive modeling of sands. The method described herein can be useful in evaluating viscous rate effects and for further refinements in sand constitutive modelling.

Conclusions

This paper describes a new experimental method based on the deformation (or flow) theory of plasticity. The method was used to determine the plastic modulus, and slopes of the plastic potential and yield surfaces during monotonic shear. The proposed method involves creating, at regular intervals, small undrained perturbations by closing the drainage valve during shear for a short time, and computing slopes and moduli at the locations where these perturbations were imposed. The proposed method was applied to an experimental program consisting of triaxial tests on loose uniformly graded sand.

For ease of interpretation the specimens were sheared while maintaining a constant mean stress, p , during shear. Note that constant p tests are not a necessity for the use of the proposed method, but simplify data interpretation because the elastic properties can be assumed to be constant during shear, and simplifies the analysis described mathematically in Eq. (7).

Results revealed that the plastic potential and yield surfaces are different, indicating non-associated flow. Furthermore, the shape of the plastic potential surfaces was qualitatively similar in shape to the Original Cam-clay model surface (Schofield and Wroth, 1968) in that the surfaces were curved, skewed to the left, and had a zero slope near the ultimate value of the q/p' ratio. Many constitutive models for sand, such as Poorooshasb, and Pietruszczak (1985), utilize Drucker-Prager type yield surfaces for which the slope of the yield surface is equal to the stress ratio during yield. The experimental results shown herein, do not support this type of yield surface.

The methods described herein constitutes a departure from the manner in which elastoplastic constitutive models are typically calibrated to match experimental data. Typically, basic parameters such as elastic constants and critical state lines are based on measurements, and other modeling constants are adjusted to provide a reasonable match between predictions and triaxial compression experiments. However, it may not be feasible to adjust the modeling constants to match the experimental data if the underlying assumptions about the yield surface shape and flow rule are incorrect. This may result in significant errors when the stress paths imposed in a simulation differ significantly from the stress paths utilized in the experiments. The methods described herein provide a simple and expeditious experimental methodology to measure the yield surface and plastic potential surface slopes, thereby enabling identification of errors in the functional form of elastoplastic constitutive models. The method is particularly useful for the calibration of the isotropic elastoplastic models that are commonly used by designers, and for the assessment and kinematic models developed from bounding surface formulations. We hope that this procedure proves useful for future constitutive model development and refinement.

Acknowledgments

This material is based upon research performed in a renovated collaboratory by the National Science Foundation under Grant No. 0963183, which is an award funded under the American Recovery and Reinvestment Act of 2009 (ARRA). The authors thank Ai Zhong for preparing the Jupyter notebook for data visualization on DesignSafe-CI.

References

Al-Tabbaa, A. and Wood, D. M., (1989), “An experimentally based "bubble' model for clay”, Numerical models in geomechanics. NUMOG III. pp. 91-99

ASCE (2010), “GeoFlorida 2010: Advances in Analyses, Modeling & Design”, Geotechnical Special Publication No.199 (GSP199), D.O. Fratta, A.J. Puppala, and B. Muhunthan (editors.), West Palm Beach, FL.

Baladi G. Y. and Rohani B. (1979), "Elastic-Plastic Model for Saturated Sand," Journal of Geotechnical Engineering, ASCE, 105, p. 465-477.

Brandenberg, S.J., Kutter, B.L., and Wilson, D.W. (2008). “Fast Stacking and Phase Corrections of Shear Wave Signals in a Noisy Environment.”, Journal of Geotechnical and Geoenvironmental Engineering, 134(8), 1154-1165.

Dafalias, Y. F. (1986), “Bounding surface plasticity. I: mathematical foundation and hypoplasticity,” Journal of Engineering Mechanics, ASCE, 112(9), 966-987.

Dafalias, Y. F. and Manzari M. T. (2004), “Simple plasticity sand model accounting for fabric change effects”, Journal of Engineering mechanics, 130(6), 622-634.

Eslami, M. (2017). “Experimental Mapping of Elastoplastic Surfaces for Sand and Cyclic Failure of low-Plasticity Fine-grained Soils.” Ph.D. Thesis, University of California, Los Angeles, CA

Eslami, M.; Brandenberg, S. J.; Zhong, A.; Pradel, D., (2017), “Triaxial Tests on Sand for Yield Surface Mapping”, DesignSafe-CI [publisher], Dataset, DOI: https://doi.org/10.17603/DS23T00

Esteva, M., Brandenberg, S. J., Eslami, M., Adair, A., Kulasekaran, S., (2016), “Modelling Natural Hazards Engineering Data to Cyberinfrastructure.” Proceedings of the SciDataCon 2016. 11-13 September 2016, Denver, Colorado. Available at: http://www.scidatacon.org/2016/sessions/104/paper/282/

Itasca Consulting Group (2011), “Computer Program FLAC 7.0”, Minneapolis, MN. www.itascacg.com.

Jones, R.M. (2009), “Deformation Theory of Plasticity”, Bull Ridge Publishing

Kuwano, R., and Jardine, R. J. (2007), “A triaxial investigation of kinematic yielding in sand”, Géotechnique, 57(7), 563-580.

Lade, P. V. (1977), “Elasto-plastic stress-strain theory for cohesionless soil with curved yield surfaces”, Int. Journal of Solids and Structures, 13(11), 1019-1035.

Lade, P. V., and Kim, M. K. (1988), “Single hardening constitutive model for frictional materials II. Yield criterion and plastic work contours”, Computers and Geotechnics, 6(1), 13-29.

Masing, G. (1926, September), “Eigenspannungen und verfestigung beim messing”, Proceedings of the 2nd Int. Congress of Applied Mechanics (Vol. 100, 332-5).

Menq, F-Y., (2003), “Dynamic properties of sandy and gravelly soils”, Dissertation at the University of Texas, Austin

Mróz, Z., Norris, V. A., and Zienkiewicz, O. C. (1979). “Application of an anisotropic hardening model in the analysis of elasto-plastic deformation of soil”, Géotechnique 29, No. 1, 1–34

Nawir, H., Tatsuoka, F. and Kuwano, R. (2003), “Viscous effects on the shear yielding characteristics of sand”, *Soils and Foundations*, Vol. 43, No. 6, pp. 33-50

Plaxis BV (2015), “Computer Program PLAXIS 2015”, Delft, Netherlands. www.plaxis.nl.

Poorooshasb, H. B., (1971), “Deformation of sand in triaxial compression”, Proc., 4th Asian Regional Conf. on SMFE, Bangkok, Vol. 1, pp. 63-66

Poorooshasb, H. B., and Pietruszczak, S. (1985), “On yielding and flow of sand; a generalized two-surface model”, Computers and Geotechnics, 1(1), 33-58.

Poorooshasb, H. B., Holubec, I., and Sherbourne, A. N. (1966) “Yielding and flow of sand in triaxial compression: Part I”, Canadian Geotechnical Journal, 3(4), 179-190.

Poorooshasb, H. B., Holubec, I., and Sherbourne, A. N. (1967), “Yielding and flow of sand in triaxial compression: Parts II and III”, Canadian Geotechnical Journal, 4(4), 376-397.

Pradel D., Ishihara K., and Gutierrez M. (1990), “Yielding and Flow of Sand under Principal Stress Axes Rotation”, Soils and Foundations, Vol. 30, No. 1, 87-99.

Pradel, D., and Lade, P. V. (1990), “Instability and plastic flow of soils. II: Analytical investigation”, Journal of Engineering Mechanics, ASCE, 116(11), 2551-2566.

Rathje, E., Dawson, C. Padgett, J.E., Pinelli, J.-P., Stanzione, D., Adair, A., Arduino, P., Brandenberg, S.J., Cockerill, T., Dey, C., Esteva, M., Haan, Jr., F.L., Hanlon, M., Kareem, A., Lowes, L., Mock, S., and Mosqueda, G. (2017), "DesignSafe: A New Cyberinfrastructure for Natural Hazards Engineering," ASCE Natural Hazards Review. DOI: 10.1061/(ASCE)NH.1527-6996.0000246

Roscoe K. H., and J. B. Burland (1968), "On the Generalised Stress-Strain Behavior of 'Wet Clay'", in Engineering Plasticity, pp. 535-609. J. Heyman and F. A. Leckie, Eds. Cambridge University Press.

Roscoe, K. H. and Schofield, A. N. (1963), "Mechanical Behaviour of an Idealised 'Wet' Clay", Proc. 2nd European Conf. on Soil Mechanics and Foundation Engineering, Wiesbaden, vol. 1, pp. 47-54

Schofield and Wroth (1968), "Critical State Soil Mechanics", McGraw-Hill.

Taiebat, M., and Dafalias, Y. F. (2008), "SANISAND: Simple anisotropic sand plasticity model", Int. Journal for Numerical and Analytical Methods in Geomechanics, 32(8), 915-948.

Tanimoto, K., and Tanaka, Y. (1986), "Yielding of soil as determined by acoustic emission", Soils and Foundations, 26(3), 69-80. Yasufuku et al, 1991

Tatsuoka, F., (2006), "Inelastic Deformation Characteristics of Geomaterial", Soil Stress-Strain Behavior: Measurement, Modeling and Analysis, A collection of papers of the Geotechnical Symposium in Rome, March 16 & 17, 2006, Springer

Tatsuoka, F., and Ishihara, K. (1974), "Yielding of sand in triaxial compression", Soils and Foundations, 14(2), 63-76.

Tatsuoka, F., and Molenkamp, F. (1983), “Discussion on yield loci for sands”, Mechanics of Granular Materials: New Models and Constitutive Relations, Elsevier Science Publisher B.V., pp.75-87.

Vermeer, P. A. (1978), “A double hardening model for sand”, Geotechnique, 28(4), 413-433.

Wood, D. M. (1990) “Soil Behaviour and Critical State Soil Mechanics”, Cambridge University Press.

Yasufuku, N., Murata, H., and Hyodo, M., (1991), “Yield characteristics of anisotropically consolidated sand under low and high stresses”, Soils and Foundations, Vol. 31, No. 1, 95-109.